Initial results from the LIGO Newtonian calibrator

Michael P. Ross [,1] Timesh Mistry [,2] Laurence Datrier [,3] Jeff Kissel,[4] Krishna Venkateswara,[1] Colin Weller,[1] Kavic Kumar [,5] Charlie Hagedorn,[1] Eric Adelberger,[1] John Lee,[1] Erik Shaw [,1] Patrick Thomas,[4] David Barker,[4] Filiberto Clara,[4] Bubba Gateley,[4] Tyler M. Guidry,[4] Ed Daw,[2] Martin Hendry,[3] and Jens Gundlach[1]

[1]*Center for Experimental Nuclear Physics and Astrophysics, University of Washington, Seattle, Washington 98195, USA*
[2]*The University of Sheffield, Sheffield S10 2TN, United Kingdom*
[3]*SUPA, University of Glasgow, Glasgow G12 8QQ, United Kingdom*
[4]*LIGO Hanford Observatory, Richland, Washington 99352, USA*
[5]*University of Maryland, College Park, Maryland 20742, USA*

The precise calibration of the strain readout of the LIGO gravitational wave observatories is paramount to the accurate interpretation of gravitational wave events. This calibration is traditionally done by imparting a known force on the test masses of the observatory via radiation pressure. Here, we describe the implementation of an alternative calibration scheme: the Newtonian calibrator. This system uses a rotor consisting of both quadrupole and hexapole mass distributions to apply a time-varying gravitational force on one of the observatory's test masses. The force produced by this rotor can be predicted to $<1\%$ relative uncertainty and is well resolved in the readout of the observatory. This system currently acts as a cross-check of the existing absolute calibration system.

I. INTRODUCTION

In recent years, gravitational wave physics has undergone a transformation from a search for a theoretical phenomenon to an observational science. The LIGO [1] and Virgo [2] gravitational wave observatories are now being used to study a growing number of astrophysical systems, including binary neutron stars [3,4] and binary black holes [5,6].

In order to extract astrophysical source parameters from the measured signals, the observatory's readout systems must be precisely calibrated across the entire sensitive frequency band (20–2000 Hz) [7,8]. The accuracy of measured gravitational wave event parameters is crucial for astrophysical population studies [9], cosmology [10,11], and probing for deviations from general relativity [12]. As such, substantial efforts have been made to yield calibration systematic errors which are less than 7% in magnitude and 4 degrees in phase for the LIGO and Virgo observatories [13,14].

A portion of reducing the systematic error relies on the accuracy and precision of the system's absolute reference, the photon calibrator (PCal) [15,16]. These systems apply a direct, known force on the end test masses via radiation pressure. Indirect options for absolute references have been used in the past, such as utilizing laser wavelength while in Michelson configurations [17,18] and various laser frequency modulation techniques [19]. However, the precision of these alternative methods has now been surpassed by the direct-force PCal systems [20,21].

Another promising direct-force absolute reference that has been previously discussed in the literature [22–27] is applying a known gravitational force to the test masses with a system of rotating masses. Such systems have recently been integrated at both the Virgo [28,29] and KAGRA [30] observatories. This paper describes the design, force modeling, first tests, and uncertainty budget of such a system for the LIGO observatories: the Newtonian calibrator (NCal).

II. BACKGROUND

A gravitational calibrator is an oscillating mass distribution that applies time-varying forces on a nearby test mass. This induces a known displacement of the test mass and thus changes the differential arm length of the observatory. These calibrators are usually designed as rotors with relatively simple geometries, which cause periodic changes in the local gravitational field as they rotate.

In the Newtonian limit, the gravitational force is the superposition of the forces caused by each of the rotor's elementary mass geometries—or equivalently, the mass multipole moments. This allows one to design a rotor which produces forces at any multiple of the rotation frequency, f. If a subgeometry of the rotor has a mass distribution that is two-fold symmetric, it will produce a force at twice the rotation frequency, $2f$. Likewise, a three-fold symmetric will produce a force at $3f$, etc. Additionally,
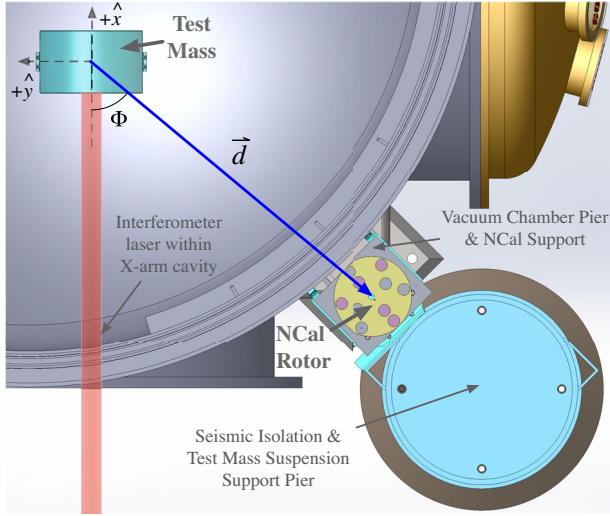
FIG. 1. Top-down view of a CAD rendering of the NCal and test mass system. The NCal is shown without its enclosing frame, shell, or motor for clarity. The test mass is shown inside its large vacuum chamber with its suspension and surrounding elements omitted. Also shown is the coordinate system used in this study along with the distance vector, $\vec{d}$, between the NCal and test mass. Note that the NCal rotor is slightly above of the x-y plane.

this allows one to disregard any subgeometry whose mass distribution does not change with rotation.

Each term has a distinct dependence on the distance between the rotor and the test mass, d. The $2f$ force caused by a two-fold symmetric quadrupole mass distribution will decrease proportional to $\sim 1/d^4$, while the force caused by a three-fold symmetric hexapole mass distribution ($3f$) will follow $\sim 1/d^5$. The force from higher multipole moments will fall off with higher orders of d.

For a fixed mass geometry, the force amplitude from each term is independent of rotation frequency. Previously,

rotors have been designed with geometries that produce signals at only $2f$ [27–29] and a mixture of both $2f$ and $3f$ [30]. The later systems have the advantage that they simultaneously inject forces at two frequencies. Furthermore, due to the different distance dependencies, this design allows for d to be measured from the observed ratio of the force amplitudes [30]. Although the rotor described in this paper was designed with the goal of exploiting this fact, our surveying achieved a significantly higher precision measurement of d than what could be reasonably achieved using the observed ratio [31,32].

III. HARDWARE

The NCal was installed at the X-end of the LIGO Hanford observatory during the commissioning break (October-November 2019) of LIGO's third observing run (O3). The system was installed on a pier just outside the test mass vacuum chamber with a custom fabricated mounting structure, as shown in Fig. 1. This location was chosen as it was the closest in-air location to the test mass considering the preexisting infrastructure. The relevant dimensions of the system are detailed in the following sections and listed in Table I.

A. Rotor

The NCal rotor, shown in Fig. 2, consists of the two basic components. The bulk of the rotor is an aluminum disk, 25.4 cm in diameter and 5.08 cm in height, with cylindrical cavities cut into it in four-fold and six-fold symmetric patterns. A set of five tungsten cylinders, of radius $r_c = 1.968$ cm and height of $l_c = 5.08$ cm, form the primary gravitating mass. These were inserted into half of the disk's cavities to form two-fold and three-fold symmetric mass distributions at radii of $r_q = 6.033$ cm and $r_h = 10.478$ cm, respectively. A similar design was first proposed in

TABLE I. Parameters of the NCal rotor and LIGO test mass, their uncertainties, and their corresponding distribution types. For parameter uncertainties described by a Gaussian distribution, the stated uncertainty indicates the σ value; for uniform, it indicates the half-width; and for uncertainties estimated numerically, the 68% credible interval; see further discussion of uncertainty in Sec. IV D.

| Parameter	Mean	Uncertainty	Distribution
Tungsten cylinder mass m	1.0558 kg	0.3 g	Gaussian
Tungsten cylinder radius r_c	1.968 cm	2.5 μm	Uniform
Tungsten cylinder length l_c	5.08 cm	5 μm	Uniform
Quadrupole radius r_q	6.033 cm	5 μm	Uniform
Hexapole radius r_h	10.478 cm	5 μm	Uniform
Test mass M	39.680 kg	10 g	Uniform
Test mass length l_{tm}	199.8 mm	0.1 mm	Uniform
Test mass radius r_{tm}	170.11 mm	0.05 mm	Uniform
Test mass flat width w_{tm}	326.5 mm	0.05 mm	Uniform
Rotor radial position ρ	1180.2 mm	2.4 mm	Numerical
Rotor angle Φ	52.24 deg	0.08 deg	Numerical
Rotor vertical position z	10.0 mm	3.0 mm	Numerical
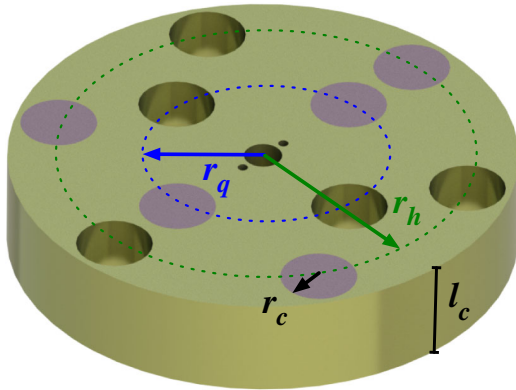
FIG. 2. CAD rendering of the NCal rotor. Solid (purple) regions indicate the holes filled with tungsten cylinders and gold regions indicating the aluminum disk and the unfilled cylindrically shaped holes. Geometrical parameters of the rotor are also highlighted for clarity.

Matone *et al.* [27] and developed for the KAGRA detector in Inoue *et al.* [30]. The disk's cavities were milled to match the diameter of the cylinders in order to minimize differential motion between the cylinders and the disk. The cylinders were cut from a single tungsten stock to minimize density differences. The aspect ratio of the cylinders was chosen to decrease the harmonic content of the applied force and increase the simplicity of the force calculations. Finally, the cylinders are restricted from moving out of the plane of the disk by an aluminum plate attached to the bottom of the disk.

B. Test mass

The observatory's test masses are cylindrical-shaped fused-silica mirrors, suspended from a nearly identical penultimate mass via four 400 μm diameter, 0.57 m long fused-silica fibers [33]. This monolithic system forms the last two stages of a quadruple pendulum system [34], which is suspended from a multistage seismic isolation system [35]. The test mass is a cylinder of radius $r_{tm} = 170.11$ mm with two vertical "flats" carved into opposite sides of the cylinder with a flat-to-flat width of $w_{tm} = 326.5$ mm [36]. Fused-silica "ears" [37] are bonded to these flats and welded to the fibers. Further small, piezoresistive tuned mass dampers are bonded to the test mass [38]. The bulk substrate of the Hanford End-X test mass was weighed in air to have a mass of 39.611 kg. The two ears and four acoustic mode dampers add a total mass of 46.05 g. Additionally, the mass of the fiber below the effective bending point adds 0.7 g. The sum of this collection of massive elements, accounting for the 22 g of buoyancy correction, yields a mass of the test mass system of $M = 39.680$ kg.

C. Drive system

Figure 3 shows the rotor, frame, and motor of the NCal system. The rotor is clamped to an aluminum shaft which
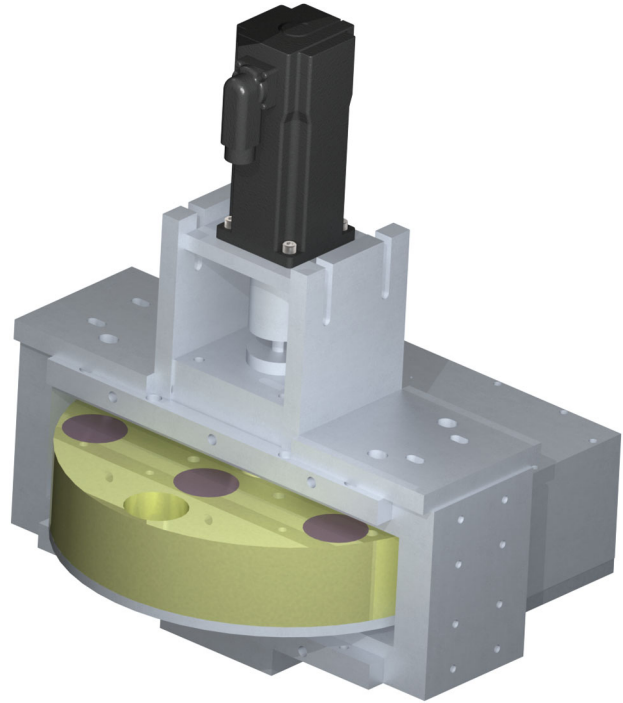

FIG. 3. CAD rendering of the rotor, frame, and motor with the front cover omitted.

runs through two sets of sealed ball bearings, one attached to the surrounding rigid frame above and below the rotor. The bearings allow the rotor to spin freely while constraining the axis of rotation.

In order to decrease vibrations of the instrument, the aluminum plate was shifted to minimize the distance between the rotation axis and the rotor's center of mass. Additionally, the upper and lower bearings were tuned to align their rotation axes. These actions decreased the $1f$ vibration to an acceptable amplitude of <0.5 m/s^2 at a rotation rate of 27.7 Hz.

A three-phase, synchronous motor is coupled to the top of the shaft and was driven by a commercially available Beckhoff motor controller. The rotation rate was locked in feedback with the motor's internal rotary encoder. This system kept the rotation frequency constant to within $<0.1\%$. A secondary rotary encoder was connected to the bottom of the shaft which independently monitored the rotation frequency. Unfortunately, the absolute phase between the encoders and the rotor masses was not aligned during installation which restricted our ability to predict the phase of the NCal forces.

IV. MODELS

As previously outlined in Sec. II, the net force acting on the test mass can be written as the sum of the forces caused by the subgeometries which make up the rotor. The force from our rotor can be broken into five terms:

$$\vec{F} = \vec{F}_{\text{Al Disk}}^{(0f)} + \vec{F}_{\text{Quad. Cyl.}}^{(2f)} + \vec{F}_{\text{Hex. Cyl.}}^{(3f)}$$
$$+ \vec{F}_{\text{Oct. Holes}}^{(4f)} + \vec{F}_{\text{Dodec. Holes}}^{(6f)} \qquad (1)$$

where the subscripts denote the subgeometry, and the superscripts indicate the lowest frequency at which each term contributes. The first term is the time-independent force due to the aluminum disk. The second and third terms are due to the tungsten cylinder masses that are, respectively, in quadrupole and hexapole configurations, and the last two terms are due to the holes in the aluminum disk which form both an octupole and a dodecapole. The contributions due to the holes can be treated as negative mass when calculating the force.

Since the observatory is insensitive to time-independent forces, we can disregard the aluminum disk term. Due to the large density difference between tungsten (19.3 g/cm^3) and aluminum (2.7 g/cm^3), the NCal primarily produces forces at $2f$ and $3f$. The missing mass of the holes also produces forces at $4f$ and $6f$. However, these are subdominant due to both the extra distance attenuation of these moments and the decreased effective mass of the holes. Additionally, the geometry inherently has higher moment contributions which are even weaker than the $4f$ and $6f$ forces. While our modeling methods are capable of accounting for these higher moments, no frequency content higher than $3f$ was observed in the measurements described in this paper. Thus only models (and subsequent comparison with measurement) for the $2f$ and $3f$ forces are discussed here.

We used three independent models to calculate the expected gravitational force between the NCal and the test mass. First, we used a point mass approximation to derive equations that can be understood analytically and quickly evaluated. To account for the full geometry of the system, we developed two other models: a finite-element simulation and a multipole method analysis. We employed

Monte Carlo methods to estimate the uncertainty on the predicted force amplitudes for each model. This begins by computing the force at a fixed orientation of the rotor with a collection of input parameters randomly sampled from their respective probability distributions. The force is then recomputed at a collection of rotor rotation angles to represent the time evolution of the force. The $2f$ and $3f$ amplitudes are then extracted by fitting to the corresponding sinusoidal functions. This is then repeated with a new randomly sampled set of parameters to yield the distributions shown in Fig. 4. This method inherently accounts for all degeneracies and nonlinearities in the force calculations.

With the NCal installed near the End-X test mass, only the x component of the force is observed by the observatory. The point mass approximation yields the x component time series for the $2f$ and $3f$ forces directly while the full geometry models provide time series containing the full harmonic content of the force in all three directions. For these methods, the $2f$ and $3f$ force amplitudes are extracted by projecting the force onto the x axis.

The two full geometry methods treat the tungsten cylinder and the holes in the aluminum disk as perfect cylinders and the test mass as a cylinder with flat sides. The aluminum disk is omitted as it does not produce a time-varying force. Additionally, the ears and suspension fibers are omitted as their geometric contributions are negligible at the current precision.

A. Point mass approximation

To find the functional form of the force, we derived analytical expressions of the $2f$ and $3f$ components by approximating each tungsten mass and the test mass as point masses at their respective centers of mass. The analytical methods used in this approximation were originally developed in Matone *et al.* [27] and furthered in Estevez *et al.* [28] for a quadrupole mass arrangement.
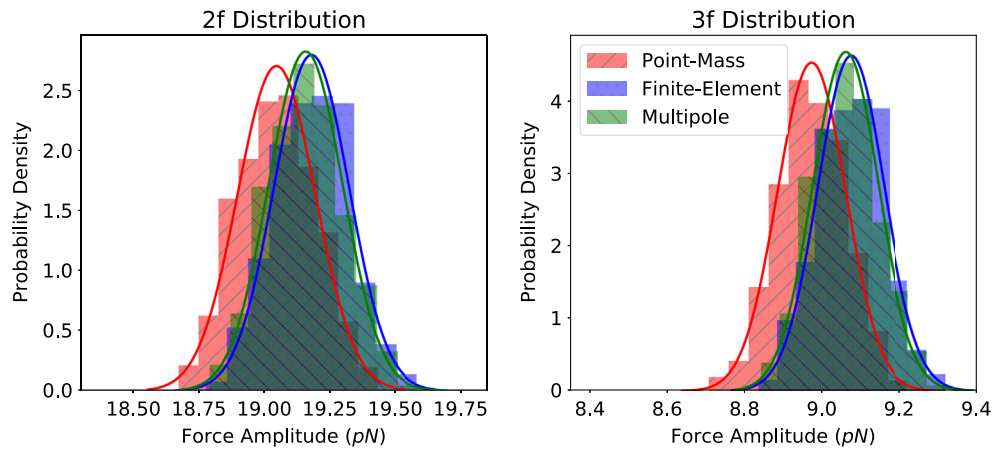

FIG. 4. Distributions of the predicted force amplitudes, $F_x^{(2f)}$ and $F_x^{(3f)}$, calculated by the point-mass, finite-element, and multipole models as well as Gaussian fits to each distribution. The small discrepancy between the point-mass model and the other two models is due to it lacking the full geometry of the system.

Here, we have extended the method to include the hexapole mass arrangement. The quadrupole representation shown here is numerically identical to the result from Estevez *et al.* [28]. The derivation of the following equations are provided in Datrier *et al.* [39].

With the assumption that the rotor is nearly in plane with the test mass ($z/d \ll 1$, $\rho \approx d$), the x component of the quadrupole force is

$$
\begin{aligned}
F_x^{(2f)} = \frac{9}{2} \frac{GMmr_q^2}{d^4} \\
\times \zeta^{-5/2} \bigg[\left(\frac{5}{6}\frac{1}{\zeta} - \frac{2}{3} \right) \cos(2\theta - \Phi) \\
+ \frac{5}{6}\frac{1}{\zeta} \cos(2\theta - 3\Phi) \bigg],
\end{aligned}
\tag{2}
$$

where G is the gravitational constant, M is the mass of the test mass, m is the mass of a tungsten cylinder, d is the distance between the rotor and test mass, Φ and z are the azimuthal and vertical positions of the rotor (as in Fig. 1), r_q is the quadrupole radius, and $\zeta = 1 + (z/d)^2$. The angle of the rotor, θ, cycles once per rotation (i.e., $\theta = 2\pi f t$).

Under the same assumptions, the x component of the hexapole force is

$$
\begin{aligned}
F_x^{(3f)} = \frac{15}{2} \frac{GMmr_h^3}{d^5} \\
\times \zeta^{-7/2} \bigg[\left(\frac{7}{8}\frac{1}{\zeta} - \frac{3}{4} \right) \cos(3\theta - 2\Phi) \\
+ \frac{7}{8}\frac{1}{\zeta} \cos(3\theta - 4\Phi) \bigg],
\end{aligned}
\tag{3}
$$

where r_h is the radius of the hexapole mass arrangement. These equations are the results of expansions to second and third order in r_q/d and r_h/d, respectively.

While these analytical expressions are approximate, they provide an consistency check of the full-geometry models and can be rapidly computed.

B. Finite-element simulation

The first full-geometry method we used is to numerically compute the force by approximating the geometry as two clouds of finite-element point masses. The force at a given θ is then simply the sum of all forces between pairs of particles, one in the "source" cloud and the other in the "test" cloud,

$$
\vec{F} = \sum_i \sum_j \frac{Gm_i M_j}{d_{ij}^2} \hat{d}_{ij},
\tag{4}
$$

where m_i is a point mass within the source cloud (the NCal), M_j is a point mass within the test cloud (the test

mass), and d_{ij} is the magnitude of the position vector from the ith point to the jth point.

A code utilizing the *PointGravity* algorithms of the newt libraries [40,41] was developed which provides the force in all three directions, as well as calculating the torques acting on the test mass about all three axes.

For each object that makes up the point clouds (tungsten cylinder or test mass), the *PointGravity* algorithm creates a Cartesian lattice of point masses with the minimum dimensions needed to contain the object. The points within the cylindrical volume of the given object are then selected out of this lattice and renormalized to account for the mass of the lost points. We chose to have an equal number of lattice points in each dimension and, through a convergence test, found that a lattice point number of 10 resulted in an acceptable inaccuracy of <0.01%.

C. Multipole analysis

In addition to the finite-element simulation, we developed a multipole-based analysis which calculates the force by breaking each object into its gravitational multipole moments. With this method, the force [42] can be found with

$$
\vec{F} = 4\pi G \sum_{l=0}^{\infty} \sum_{m=-l}^{l} \frac{1}{2l+1} Q_{lm} \nabla q_{lm},
\tag{5}
$$

where Q_{lm} is the "outer" multipole, and q_{lm} is the "inner" multipole. For our geometry, the inner multipole corresponds to the NCal while the outer corresponds to the test mass.

The forces along all three axes were calculated using the *Multipole* algorithms of the newt libraries [41]. These libraries construct the system's geometry from a collection of elementary solids whose multipole moments have been analytically determined [43,44]. The forces between the rotor and the test mass are then calculated using methods based on a wide collection of literature sources [42,45,46].

To numerically evaluate the force using Eq. (5), an upper cutoff for the l sum must be imposed. For our analysis, this was chosen to be $l = 11$. Moments higher than $l = 11$ only contribute significantly to frequencies greater than $11f$.

D. Parameter uncertainty

The estimated force and uncertainty for each model are determined numerically using Monte Carlo methods with parameters defined by a selection of probability distributions. The distribution type and defining characteristics are listed in Table I and motivated below.

Geometric parameters of the cylinders, r_c, l_c, r_q, and r_h, were determined with a single micrometer measurement with a known precision. For these parameters, we assigned a uniform distribution centered on the measured value and bounded by the precision. Geometric parameters of the test

mass, l_{tm}, r_{tm}, and w_{tm} are determined from tightly controlled vendor specifications and are also assigned uniform probability distributions bounded by their respective tolerances.

The force models assume an equal mass, m, for all five tungsten cylinders. We take m to be a Gaussian distribution with a central value equal to the mean of the measured masses and a σ value equal to their standard deviation. In contrast, since there is only one test mass, we set the distribution for M in a similar way as geometric parameters of the cylinders: a uniform probability distribution bounded by the estimated precision.

Surveying equipment was used to determine the position of the NCal frame and the front surface of the test mass with respect to monuments located on the floor and walls of the observatory. For the NCal, the frame location was combined with a CAD model confirmed by bench-top measurements to give the position of the rotor's center of mass. Similarly, the in-vacuum position of the test mass center of mass was found by shifting the x-position measurement of the front surface by half of the test mass thickness, and the z-position measurement was altered to account for the lack of buoyancy in vacuum. Finally, these two positions were subtracted to yield the positions, ρ, Φ, and z, of the NCal in coordinates centered on the test mass center of mass. As the process involved several nonlinear transformations, the probability distribution of the relative position was calculated numerically through Monte Carlo methods. Further details of the surveying and position calculations can be found in Ref. [31].

Individual parameter contributions to the force uncertainty are discussed in the Appendix B.

E. Model comparison

Histograms of the distribution of force amplitudes from each model are shown in Fig. 4. The distributions are computed from a set of 800 samples for each model. The number of samples was chosen to maximize the accuracy of the distribution while minimizing the computational cost for the finite-element analysis. Each model's distribution is fit to a Gaussian whose mean and σ values are taken to be the estimated value and uncertainty, respectively, and are reported in Table II.

TABLE II.   Predicted force amplitudes and uncertainties extracted from the distributions shown in Fig. 4 for the finite-element, multipole, and point-mass models.

Model	$F_x^{(2f)}$ (pN)	$F_x^{(3f)}$ (pN)
Finite element	$19.18^{\pm 0.14}_{(\pm 0.75\%)}$	$9.07^{\pm 0.09}_{(\pm 0.95\%)}$
Multipole	$19.16^{\pm 0.14}_{(\pm 0.74\%)}$	$9.06^{\pm 0.09}_{(\pm 0.94\%)}$
Point mass	$19.04^{\pm 0.15}_{(\pm 0.76\%)}$	$8.97^{\pm 0.09}_{(\pm 0.95\%)}$

All three models provide almost identical levels of uncertainty at ∼0.75% and ∼0.95% for the $2f$ and $3f$ force amplitudes, respectively. However, the point mass approximation predicts a lower mean value than the other two models. This discrepancy is due to the point mass approximation's improper treatment of the geometry of the system. While the finite-element model accurately captures the full system, we take the multipole model to be the most robust model as it captures the entire geometry of the system and utilizes exact solutions for the multipole moments. As such, we use the results of the multipole analysis to compare with measurements while the other two models are only used to verify the accuracy of the multipole force predictions.

V. MEASUREMENTS

On December 4, 2019, gravitational forces were injected with the NCal while the observatory was in its observation-ready noise state. The rotor rotation frequency, f, was stepped through five values ranging from 4 to 10 Hz which injected forces between 8 to 30 Hz. Explicit values for f, $2f$, and $3f$ are listed in Table IV. Investigations into the impact of the NCal electronics in addition to the vibrational noise contributions found no significant increase in the observatory's noise performance during the operation of the NCal. For further discussion of extraneous couplings, see Sec. VI.

The observatory's differential strain readout, h, was recorded continuously during the NCal injections. Any observed strain at the expected $2f$ and $3f$ frequencies was attributed to the force by the NCal on the test mass. As such, we convert the observed strain into force in the x direction with

$$F_x = Lh/S, \tag{6}$$

where h is the strain output, L is the arm length, and S is the magnitude of the force-to-displacement response of the test mass suspension system.

Figure 5 shows the collection of amplitude spectra of the force on the test mass during the injections. Each overlaid color amplitude spectra correspond to a different rotor rotation frequency. Although these spectra are not used in our results, they convey the sensitivity of the observatory during the NCal injections. The $2f$ and $3f$ forces are clearly resolved for most rotation frequencies, and the signal-to-noise improves with frequency. The $3f$ signal from $f = 5.17$ Hz and $2f$ signal from $f = 7.80$ Hz intentionally overlap. No additional features or broadband noise were observed during these injections. The $4f$ and $6f$ forces caused by the holes in the rotor may be resolved with future, long duration injections. Artifacts, unrelated to the NCal injections, can also be seen in Fig. 5. First, the strain below 10 Hz is to be ignored as it is aggressively high passed to aide astrophysical search algorithms.
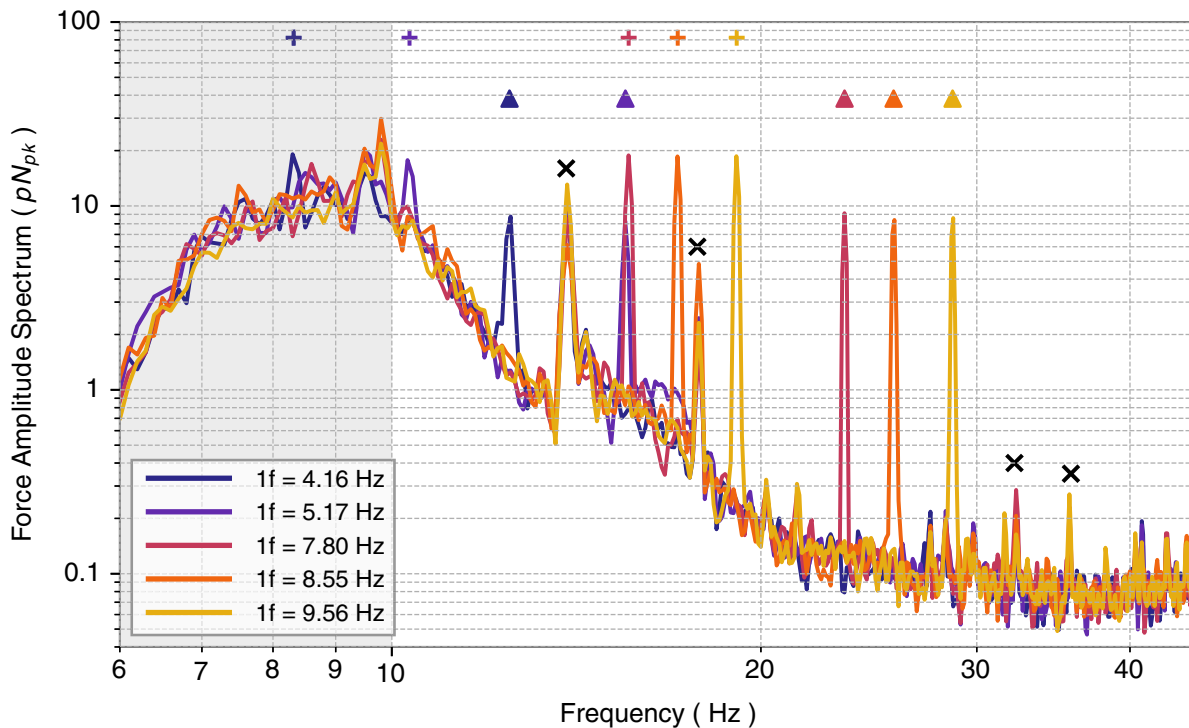
FIG. 5. The collection of amplitude spectra of the observed force during successive NCal injections. Each colored trace represents a different injection when the NCal was rotating at the corresponding $1f$ rotation frequency. As visual aides, similarly colored plus- and triangle-shaped markers indicate the location of the $2f$ and $3f$ frequencies at arbitrary amplitudes. Black cross-shaped markers highlight ever-present spectral features that are unrelated to the NCal injection. The gray shaded region indicates the frequency band where the strain readout is aggressively high passed and thus should be ignored.

Additionally, there are ever-present spectral features that must be avoided when choosing injection frequencies.

The force amplitudes are extracted using least squares spectral analysis [47]. This consists of fitting the strain readout in the time domain using linear least squares to the following sinusoidal function:

$$h(t) = a_2 \cos(2\pi 2 f t) + b_2 \sin(2\pi 2 f t)$$
$$+ a_3 \cos(2\pi 3 f t) + b_3 \sin(2\pi 3 f t), \quad (7)$$

where a_i and b_i are the cosine and sine amplitudes at the respective frequencies, f is the rotor rotation frequency, and t is time. The data were cut into sections with lengths equal to 20 $1f$ periods. Each cut was then fit independently, and the extracted sine and cosine amplitudes were averaged before being combined in quadrature to yield a strain amplitude,

$$h(f_i) = \sqrt{a_i^2 + b_i^2}. \quad (8)$$

Finally, the extracted strain amplitudes were then converted to force using Eq. (6). The uncertainty on the observed force amplitude was calculated by propagating the standard deviation of the sine and cosine amplitudes through Eq. (6).

The least squares spectral analysis method has multiple benefits over a traditional Fourier-based spectral analysis. First, it guarantees that the amplitude is extracted for the frequency of interest (i.e., frequency bins are centered on the frequencies of interest). Additionally, the extracted sine and cosine amplitudes are guaranteed to be Gaussian distributed as long as the measured strain is also Gaussian. The statistical uncertainty can also be extracted directly from the observed distribution of amplitudes. Lastly, there are no correction factors that need be included which decreases the nuance of the analysis and removes possible sources of error.

VI. SYSTEMATICS AND TOTAL UNCERTAINTY

In addition to the gravitational force from the NCal, the observed force is influenced by a variety of effects that must be accounted for to accurately extract the measured force. These effects include indirect gravitational coupling, nongravitational coupling, and distortion due to the observatory's strain readout. These influences can be taken into account in a few ways: by adding a correction to either the measurement or the model or by expanding the uncertainty in either to account for these contributions. Due to the nature of these systematics and extraneous couplings, we chose to correct and expand the uncertainty of the

TABLE III.   Comparison between the amplitude uncertainty in the model (Model: $F_x^{(2f)}$ and $F_x^{(3f)}$), the measured force (Meas: Statistical), the various systematics (Sys), and the total measured and systematic uncertainty (Meas & Sys). The ratios between the contributions and the multipole model are shown in square braces in percent. Contributions which are frequency dependent are shown as a range between their minimun-maximum values.

Source	Correction (pN), [ratio relative to model, (%)]	Uncertainty (pN), [ratio relative to model, (%)]
	$2f$	
Model: $F_x^{(2f)}$	…	0.14, [0.74]
Meas: Statistical	…	0.21–2.33 [1.09–12.16]
Sys: Penultimate	…	0.007–0.033 [0.04–0.17]
Sys: Magnetic	…	0.04 [0.21]
Sys: S	…	0.022–0.064 [0.11–0.34]
Sys: Torque	0.339 [1.77]	0.026 [0.14]
Meas & Sys	…	0.22–2.33 [1.12–12.17]
	$3f$	
Model: $F_x^{(3f)}$	…	0.09 [0.94]
Meas: Statistical	…	0.24–0.57 [2.64–6.31]
Sys: Penultimate	…	0.0002–0.0074 [0.002–0.081]
Sys: Magnetic	…	0.04 [0.44]
Sys: S	…	0.005–0.024 [0.05–0.26]
Sys: Torque	0.199 [2.19]	0.015 [0.17]
Meas & Sys	…	0.24–0.57 [2.69–6.34]

measurement. The corrections and uncertainties for each systematic are shown in Table III along with the measurement and model uncertainties.

A. Indirect gravitational coupling

The NCal rotor not only gravitationally attracts the test mass but also pulls on the rest of the suspension system. The penultimate mass is the next closest component of the suspension, 602 mm above the test mass center of mass [48], and transmits motion to the test mass through the suspension fibers. This coupling path was studied using the finite-element simulation described in Sec. IV B. This simulation found that—aside from the quadrupole influence at 10.34 Hz—the penultimate contributions are less than 0.1% of the expected forces [49]. Even at 10.34 Hz, the coupling increases to only ~0.17%. Since this is much less than the measurement statistical uncertainty, we expanded each measurement uncertainty by the corresponding penultimate mass contribution. This contribution is labeled in Table III as Sys: Penultimate The forces on the rest of the suspension are expected to be negligible due to the increased distance from the NCal rotor.

B. Nongravitational coupling

One concern that may skew the measured force is that the NCal rotor and test mass could be coupled through magnetic effects. Using existing magnetic coupling measurements for

the test mass [50] and a collocated magnetometer, we constrained the force due to magnetic coupling to be <0.04 pN across the frequency band of interest [51]. To account for this, we add a conservative uncertainty of 0.04 pN to each measured force. This contribution is labeled as Sys: Mag in Table III. With dedicated magnetic coupling measurements and mitigation, we expect this contribution to decrease for future studies.

Another nongravitational coupling that may influence the measurements is the transmission of vibrations caused by the NCal. Vibrations caused by the NCal rotor can couple into the strain measurements through the seismic isolation system as well as through scattered light. The frequency region of existing vibrational coupling measurements [50] do not extend to our band of interest. As such, we were unable to constrain the vibrational contribution to the observed force. However, accelerometers located near the rotor did not observe any change in the ambient vibrations while the NCal was rotating [51]. Since ambient vibrations are known to not contribute strongly to the observatory's noise level [50], we expect that vibrations are not a significant source of the observe force. This will be studied in detail with future dedicated vibration coupling injections and measurements.

C. Detector readout systematics

In addition to forces on the suspension system, the NCal rotor applies torques to the masses. Again due to the increased distance dependence of the gravitational interactions, the torques on the test mass are expected to be significantly larger than those on the rest of the suspension system. These torques couple into the strain measurements due to the interferometric beam being offset from the center of rotation of the test mass. During O3, the beam was offset by 13.2 ± 1 mm in the y direction and -15.7 ± 1 mm in the z direction. This offset causes the angle change due to torques about the y and z axes (pitch and yaw) to cause arm length changes. This arm length change is then interpreted as force in our measurements. The torque to force coupling was also studied using the finite-element simulation described in Sec. IV B [52]. The apparent force due to both torques summed together is 0.339 ± 0.026 pN for the $2f$ and 0.199 ± 0.015 pN for the $3f$. We shift each measured force by the corresponding amount, accounting for relative phase, to remove this contribution and add the uncertainty to each measurement point. This shift is the only correction we apply as its phase is well known from the model. The corrections and corresponding uncertainties are listed in Table III as Sys: Torque. The torques on the rest of the suspension chain are expected to be negligible as they will be attenuated by the extra distance.

As discussed in Eq. (6), the strain readout is converted to force via the test mass force-to-displacement transfer function S. Above 10 Hz, we approximate the test mass as a free mass, $S = -1/(M(2\pi f)^2)$. Comparing this to a

TABLE IV.   Measured force amplitudes, $F_x^{(2f)}$ and $F_x^{(3f)}$, with corrections applied for extraneous couplings at the expected quadrupole $2f$ and hexapole $3f$ frequencies.

$1f$ (Hz)	$2f$ (Hz)	$F_x^{(2f)}$ (pN)	$3f$ (Hz)	$F_x^{(3f)}$ (pN)
4.16	8.32	...	12.45	$8.79^{\pm0.32}_{\pm3.61\%}$
5.17	10.34	$16.59^{\pm2.33}_{\pm14.05\%}$	15.51	$8.98^{\pm0.46}_{\pm5.07\%}$
7.80	15.60	$19.28^{\pm0.30}_{\pm1.56\%}$	23.40	$9.12^{\pm0.37}_{\pm4.10\%}$
8.55	17.11	$19.10^{\pm0.47}_{\pm2.44\%}$	25.66	$9.01^{\pm0.57}_{\pm6.36\%}$
9.56	19.11	$19.28^{\pm0.21}_{\pm1.12\%}$	28.67	$9.15^{\pm0.24}_{\pm2.66\%}$

full model of the complete dynamics of the suspension shows this adds a frequency-dependent error of no more than 0.4% above 10 Hz [53]. The uncertainty of the measured force has been expanded to encompass this expected error and is listed in Table III as Sys: S.

D. Results and total uncertainty

The measured force amplitudes are listed in Table IV and shown in Fig. 6 alongside the predictions from each model described in Sec. IV. The measured force is consistent with the frequency-independent predictions at all frequencies with the only excursion being at 10.34 Hz, where the detector noise is worse and many of the systematics have their largest effect. Due to the limited time spans of the injections, the statistical uncertainty for every measurement is larger than the model uncertainty.

As the distributions of the different uncertainty contributions are unknown, we assign them Gaussian distributions with σ values of the uncertainties in Table III. Since the various extraneous couplings are linear terms added to the measured force, and are expected to be uncorrelated, the uncertainty for each measured force is taken to be the quadrature sum of the relevant uncertainties.
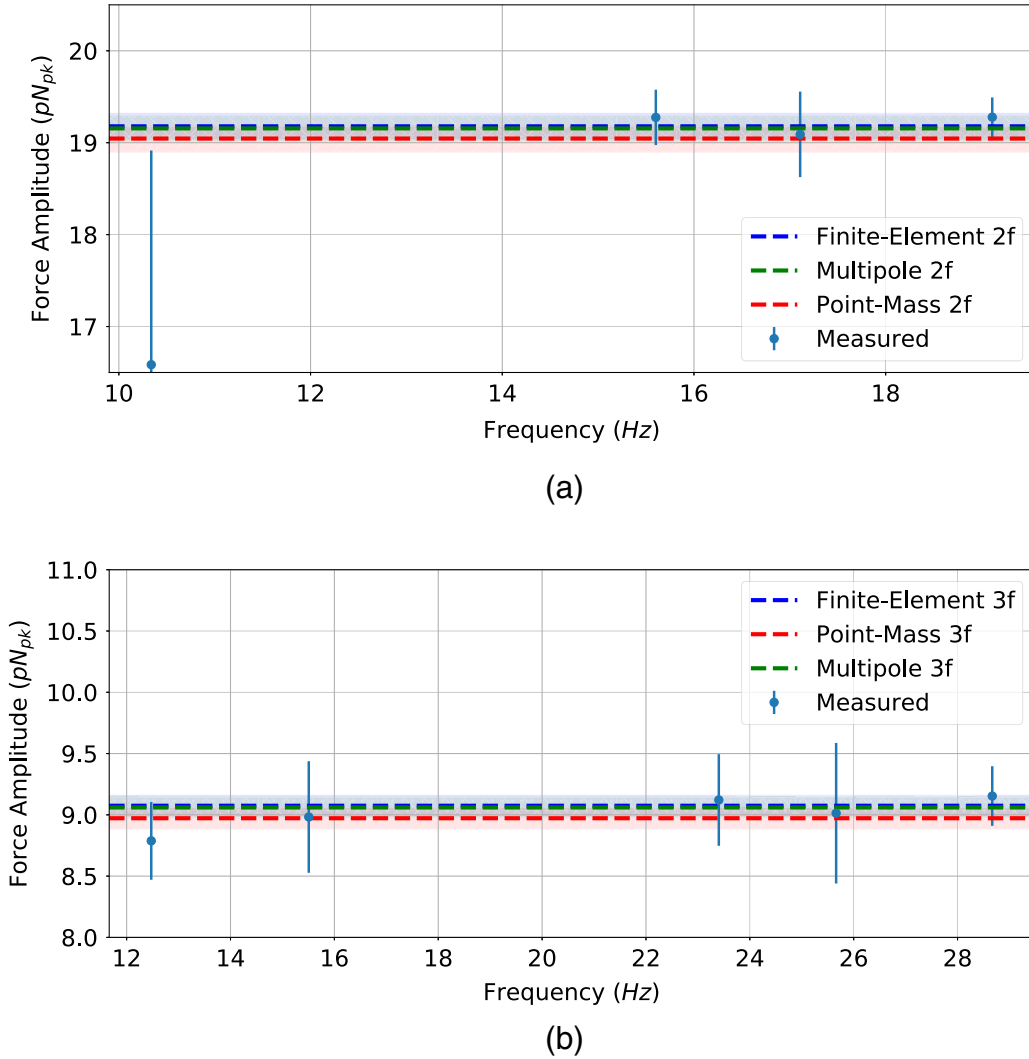

(a)

(b)

FIG. 6.   (a) Force exerted by the quadrupole mass arrangement, $F_x^{(2f)}$, as measured by the detector compared with the frequency-independent values predicted by the molecules from Sec. IV. (b) Force exerted by the hexapole mass arrangement, $F_x^{(3f)}$, as measured by the detector compared with the frequency-independent values predicted by the molecules from Sec. IV.

The torque and the penultimate contributions are covariant with model uncertainty since we used the models to evaluate them all. We do not account for these covariances as they are expected to be smaller than the corresponding variances and significantly smaller than the measurement uncertainties.

VII. ABSOLUTE CALIBRATION

One immediate utility of these measurements is to act as a cross-check for the existing estimate of the systematic error in the observatory's strain readout. In Sun *et al.* [13], many reference measurements are concatenated to yield a model of the detector's strain response, R_{model}. The resulting model may be compared against the response measured with a direct force absolute reference, R_{ref}. The ratio of these two form a frequency-dependent complex valued function that represents the systematic error in R_{model},

$$\eta_R = \frac{R_{ref}}{R_{model}}. \tag{9}$$

Ideally, if no systematic error is present, then $\eta_R = 1$. Figure 7 shows the systematic error as measured by the NCal system along with the modeled systematic error shown in Sun *et al.* [13]. Here, the NCal systematic error magnitude is determined by taking the ratio of the modeled forces as predicted by the multipole model and the observed force corrected for systematics at each $2f$ and $3f$ frequency. Equation (6) shows that the ratio of forces is the same as the ratio of strains. Since we do not know the absolute phase of the NCal rotor, we are restricted to only evaluating the magnitude of the systematic error. The NCal results are consistent with the modeled systematic error at all frequencies.
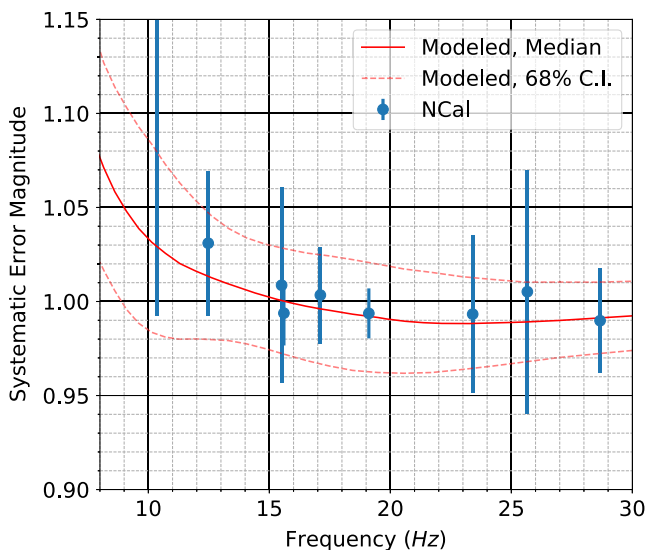

FIG. 7. Comparison between the modeled systematic error magnitude and systematic error as measured by the NCal.

By combining the modeled systematic error, the measured force, and the simulations of the geometry, these measurements also allow a low-precision measurement of the gravitational constant detailed in Appendix A.

VIII. CONCLUSION

We have built and installed a gravitational calibration system at the LIGO Hanford detector which can reliably inject forces at known frequencies. These forces can be predicted to <1% relative uncertainty and have provided an independent check of the existing absolute calibration system.

In future work, we plan to analyze a set of simultaneous injections with both the NCal and the PCal systems. This will allow for two independent, absolute calibrations of the strain readout of the observatory which can be combined for increased precision.

Although our current results are limited by the statistical uncertainty, we plan to decrease the various systematic effects with the goal of minimizing the total uncertainty in future NCal calibration injections. The influence of the torques on the force measurements can be decreased by altering the location of the NCal rotor and minimizing the interferometric beam offset on the test mass. We also plan to conduct dedicated environmental coupling measurements and mitigation to improve the magnetic and vibrational uncertainties.

The precision of the force model limits the NCal's absolute calibration independent of systematics. The current NCal prototype's model uncertainty is dominated by the precision of position surveying. With future upgrades (involving multiple rotors), we hope to circumvent the need for this surveying and thus decrease the uncertainty of the force model.

Additionally, future iterations of this instrument may allow novel gravitational experiments such as searches for non-Newtonian gravity [54], terrestrial measurements of Shapiro delay [55,56], and measurements of the gravitational constant [57].

ACKNOWLEDGMENTS

APPENDIX A: GRAVITATIONAL CONSTANT MEASUREMENT

In addition to the calibration results discussed here, the NCal system allows a unique measurement of the gravitational constant, G [57]. The preexisting calibration system [15] allows the force acting on the test mass to be measured precisely while the simulations described in Sec. IV B can account for the mass distributions.

The observed forces at the different rotation frequencies were treated as independent measurements of G once they were corrected for the known systematic error. These corrected measurements were then averaged to yield

$$G = (6.56 \pm 0.41) \times 10^{-11} \text{ m}^3 \text{ kg}^{-1} \text{ s}^{-2}. \quad \text{(A1)}$$

Although not competitive with previous measurements [58], this is the first gravitational constant measurement utilizing a gravitational wave detector. We expect the precision of this measurement to increase with improvements to metrology of the geometry and to the accuracy of the force measurements. However, it is unlikely that even future results with this technique will be competitive with other existing apparatus (torsion balances, etc.).

APPENDIX B: MODEL UNCERTAINTY CONTRIBUTION ANALYSIS

As discussed in Sec. IV, the uncertainty of the modeled force was numerically evaluated via Monte Carlo methods in order to account for nonlinearities and parameter degeneracies. However, to assess the uncertainty contributions from each model parameter separately, we calculated the difference in the force when each parameter was varied independently by its respective uncertainty. This was done with only the multipole method; however, we expect similar results from either the analytical calculations or the finite-element analysis. The results of this analysis are shown in Table V along with the quadrature sum of the individual contributions. It is apparent that the primary contribution to force uncertainty is the relative position between the rotor and the test mass.

Estimating the total force uncertainty with the quadrature sum does not account for any nonlinearities that are inherent in the force calculation or covariance between the parameters. Thus, the total uncertainty shown in Table V differs slightly from the results of our Monte Carlo calculations.

TABLE V. Individual uncertainty contributions for force applied by the NCal along with the quadrature sum of the contributions.

Parameter	Mean	Uncertainty	$2f$ Uncertainty contribution (pN)	$3f$ Uncertainty contribution (pN)
Cylinder mass	1.0558 kg	0.3 g	5.44×10^{-3} (0.03%)	2.57×10^{-3} (0.03%)
Test mass	39.680 kg	10 g	4.83×10^{-3} (0.03%)	2.28×10^{-3} (0.03%)
Cylinder height	5.08 cm	5 μm	2.01×10^{-6} ($\sim 10^{-5}$%)	1.21×10^{-6} ($\sim 10^{-5}$%)
Cylinder radius	1.968 cm	2.5 μm	1.16×10^{-6} ($\sim 10^{-5}$%)	7.04×10^{-7} ($\sim 10^{-5}$%)
Test mass length	199.8 mm	0.1 mm	4.78×10^{-5} ($\sim 10^{-4}$%)	2.71×10^{-5} ($\sim 10^{-4}$%)
Test mass radius	170.11 mm	0.05 mm	6.92×10^{-5} ($\sim 10^{-4}$%)	3.87×10^{-5} ($\sim 10^{-4}$%)
Test mass width	326.5 mm	0.05 mm	1.46×10^{-4} ($\sim 10^{-3}$%)	9.06×10^{-5} ($\sim 10^{-3}$%)
Rotor position (x)	722.8 mm	2.5 mm	8.77×10^{-2} (0.46%)	5.55×10^{-2} (0.61%)
Rotor position (y)	933.0 mm	1.5 mm	8.19×10^{-2} (0.43%)	4.68×10^{-2} (0.52%)
Rotor position (z)	10.0 mm	3.0 mm	3.23×10^{-3} (0.02%)	1.95×10^{-3} (0.02%)
Quadruple radius	6.033 cm	5 μm	3.18×10^{-3} (0.02%)	1.62×10^{-15} ($\sim 10^{-14}$%)
Hexapole radius	10.478 cm	5 μm	5.82×10^{-14} ($\sim 10^{-13}$%)	1.30×10^{-3} (0.01%)
			Force (pN)	Sum of contributions (pN)
$F_x^{(2f)}$			19.16	0.12 (0.63%)
$F_x^{(3f)}$			9.06	0.07 (0.81%)

[1] J. Aasi *et al.*, Advanced LIGO, Classical Quantum Gravity **32**, 074001 (2015).

[2] F. Acernese *et al.*, Advanced Virgo: A second-generation interferometric gravitational wave detector, Classical Quantum Gravity **32**, 024001 (2015).

[3] B. P. Abbott *et al.* (The LIGO Scientific and the Virgo Collaborations), GW170817: Observation of Gravitational Waves from a Binary Neutron Star Inspiral, Phys. Rev. Lett. **119**, 161101 (2017).

[4] B. P. Abbott *et al.*, GW190425: Observation of a compact binary coalescence with total mass ~ 3.4 m$_\odot$, Astrophys. J. **892**, L3 (2020).

[5] B. P. Abbott *et al.*, GWTC-1: A Gravitational-Wave Transient Catalog of Compact Binary Mergers Observed by LIGO and Virgo During the First and Second Observing Runs, Phys. Rev. X **9**, 031040 (2019).

[6] R. Abbott *et al.*, GW190412: Observation of a binary-black-hole coalescence with asymmetric masses, Phys. Rev. D **102**, 043015 (2020).

[7] S. Vitale, C.-J. Haster, L. Sun, B. Farr, E. Goetz, J. Kissel, and C. Cahillane, Physical approach to the marginalization of LIGO calibration uncertainties, Phys. Rev. D **103**, 063016 (2021).

[8] E. Payne, C. Talbot, P. D. Lasky, E. Thrane, and J. S. Kissel, Gravitational-wave astronomy with a physical calibration model, Phys. Rev. D **102**, 122004 (2020).

[9] R. Abbott, T. D. Abbott, S. Abraham, F. Acernese, K. Ackley, A. Adams, C. Adams, R. X. Adhikari, V. B. Adya, C. Affeldt *et al.*, Population properties of compact objects from the second LIGO-Virgo gravitational-wave transient catalog, Astrophys. J. Lett. **913**, L7 (2021).

[10] LIGO Scientific, Virgo, 1M2H, Dark Energy Camera GW-EM, DES, DLT40, Las Cumbres Observatory, VINROUGE, MASTER Collaborations *et al.*, A gravitational-wave standard siren measurement of the hubble constant, Nature (London) **551**, 85 (2017).

[11] B. P. Abbott, R. Abbott, T. D. Abbott, S. Abraham, F. Acernese, K. Ackley, C. Adams, R. X. Adhikari, V. B. Adya, C. Affeldt *et al.*, A gravitational-wave measurement of the hubble constant following the second observing run of Advanced LIGO and Virgo, Astrophys. J. **909**, 218 (2021).

[12] R. Abbott, T. D. Abbott, S. Abraham, F. Acernese, K. Ackley, A. Adams, C. Adams, R. X. Adhikari, V. B. Adya, C. Affeldt *et al.*, Tests of general relativity with binary black holes from the second LIGO-Virgo gravitational-wave transient catalog, Phys. Rev. D **103**, 122002 (2021).

[13] L. Sun *et al.*, Characterization of systematic error in Advanced LIGO calibration, Classical Quantum Gravity **37**, 225008 (2020).

[14] D. Estevez, B. Mours, L. Rolland, and D. Verkindt, Online h (t) reconstruction for Virgo O3 data: Start of O3, Technical Report No. VIR-0652B-19, Virgo, 2019.

[15] S. Karki, D. Tuyenbayev, S. Kandhasamy, B. P. Abbott, T. D. Abbott, E. H. Anders, J. Berliner, J. Betzwieser, C. Cahillane, L. Canete *et al.*, The Advanced LIGO photon calibrators, Rev. Sci. Instrum. **87**, 114503 (2016).

[16] D. Estevez, P. Lagabbe, A. Masserot, L. Rolland, M. Seglar-Arroyo, and D. Verkindt, The Advanced Virgo photon calibrators, Classical Quantum Gravity **38**, 075007 (2021).

[17] J. Abadie *et al.*, Calibration of the LIGO gravitational wave detectors in the fifth science run, Nucl. Instrum. Methods Phys. Res., Sect. A **624**, 223 (2010).

[18] T. Accadia, F. Acernese, F. Antonucci, S. Aoudia, K. G. Arun, P. Astone, G. Ballardin, F. Barone, M. Barsuglia, T. S. Bauer *et al.*, Virgo calibration and reconstruction of the gravitationnal wave strain during vsr1, J. Phys. **228**, 012015 (2010).

[19] E. Goetz and R. L. Savage, Calibration of the LIGO displacement actuators via laser frequency modulation, Classical Quantum Gravity **27**, 215001 (2010).

[20] E. Goetz, R. L. Savage, J. Garofoli, G. Gonzalez, E. Hirose, P. Kalmus, K. Kawabe, J. Kissel, M. Landry, B. O'Reilly *et al.*, Accurate calibration of test mass displacement in the LIGO interferometers, Classical Quantum Gravity **27**, 084024 (2010).

[21] B. P. Abbott, R. Abbott, T. D. Abbott, M. R. Abernathy, K. Ackley, C. Adams, P. Addesso, R. X. Adhikari, V. B. Adya, C. Affeldt *et al.*, Calibration of the Advanced LIGO detectors for the discovery of the binary black-hole merger gw150914, Phys. Rev. D **95**, 062003 (2017).

[22] H. Hirakawa, K. Tsubono, and K. Oide, Dynamical test of the law of gravitation, Nature (London) **283**, 184 (1980).

[23] K. Kuroda and H. Hirakawa, Experimental test of the law of gravitation, Phys. Rev. D **32**, 342 (1985).

[24] N. Mio, K. Tsubono, and H. Hirakawa, Experimental test of the law of gravitation at small distances, Phys. Rev. D **36**, 2321 (1987).

[25] P. Astone, M. Bassan, S. Bates, R. Bizzarri, P. Bonifazi, R. Cardarelli, G. Cavallari, E. Coccia, A. Degasperis, D. De Pedis *et al.*, Evaluation and preliminary measurement of the interaction of a dynamical gravitational near field with a cryogenic gravitational wave antenna, Z. Phys. C Part. Fields **50**, 21 (1991).

[26] P. Astone, M. Bassan, R. Bizzarri, P. Bonifazi, L. Brocco, P. Carelli, E. Coccia, C. Cosmelli, A. Degasperis, S. Frasca *et al.*, Experimental study of the dynamic newtonian field with a cryogenic gravitational wave antenna, Eur. Phys. J. C Part. Fields **5**, 651 (1998).

[27] L. Matone, P. Raffai, S. Márka, R. Grossman, P. Kalmus, Z. Márka, J. Rollins, and V. Sannibale, Benefits of artificially generated gravity gradients for interferometric gravitational-wave detectors, Classical Quantum Gravity **24**, 2217 (2007).

[28] D. Estevez, B. Lieunard, F. Marion, B. Mours, L. Rolland, and D. Verkindt, First tests of a newtonian calibrator on an interferometric gravitational wave detector, Classical Quantum Gravity **35**, 235009 (2018).

[29] D. Estevez, B. Mours, and T. Pradier, Newtonian calibrator tests during the Virgo O3 data taking, Classical Quantum Gravity **38**, 075012 (2021).

[30] Y. Inoue, S. Haino, N. Kanda, Y. Ogawa, T. Suzuki, T. Tomaru, T. Yamanmoto, and T. Yokozawa, Improving the absolute accuracy of the gravitational wave detectors by combining the photon pressure and gravity field calibrators, Phys. Rev. D **98**, 022005 (2018).

[31] T. Mistry, M. Ross, L. Datrier, J. Oberling, J. Kissel, and E. Daw, NCal prototype H1 surveying distance measurement, LIGO DCC, 2021, https://dcc.ligo.org/LIGO-T2000417/public.

[32] M. P. Ross, J. Kissel, L. Datrier, and T. Mistry, NCal ratio method analysis, LIGO DCC, 2021, https://dcc.ligo.org/LIGO-T2100066/public.

[33] A. V. Cumming, A. S. Bell, L. Barsotti, M. A. Barton, G. Cagnoli, D. Cook, L. Cunningham, M. Evans, G. D. Hammond, G. M. Harry *et al.*, Design and development of the Advanced LIGO monolithic fused silica suspension, Classical Quantum Gravity **29,** 035003 (2012).

[34] S. M. Aston, M. A. Barton, A. S. Bell, N. Beveridge, B. Bland, A. J. Brummitt, G. Cagnoli, C. A. Cantley, L. Carbone, A. V. Cumming *et al.*, Update on quadruple suspension design for Advanced LIGO, Classical Quantum Gravity **29,** 235004 (2012).

[35] F. Matichard, B. Lantz, R. Mittleman, K. Mason, J. Kissel, B. Abbott, S. Biscans, J. McIver, R. Abbott, S. Abbott *et al.*, Seismic isolation of Advanced LIGO: Review of strategy, instrumentation and performance, Classical Quantum Gravity **32,** 185003 (2015).

[36] C. Torrie, aLIGO, coc end test mass (etm) substrate, LIGO DCC, 2008, https://dcc.ligo.org/LIGO-D080658/public.

[37] M. van Veggel, Advanced LIGO, suspension, etm/itm test mass, production ear, LIGO DCC, 2008, https://dcc.ligo.org/LIGO-D080751/public.

[38] S. Biscans, S. Gras, C. D. Blair, J. Driggers, M. Evans, P. Fritschel, T. Hardwick, and G. Mansell, Suppressing parametric instabilities in LIGO using low-noise acoustic mode dampers, Phys. Rev. D **100,** 122003 (2019).

[39] L. Datrier, J. Kissel, T. Mistry, and M. Ross, Review of NCal analytic force estimates, mathematical details, LIGO DCC, 2020, https://dcc.ligo.org/LIGO-T2000238/public.

[40] C. A. Hagedorn, A sub-millimeter parallel-plate test of gravity, Ph.D thesis, University of Washington, January, 2015.

[41] C. Hagedorn and J. G. Lee, Newt (newtonian eot-wash toolkit), GitHub, 2021, https://github.com/4kbt/NewtonianEotWashToolkit.

[42] J. Stirling, Multipole calculation of gravitational forces, Phys. Rev. D **95,** 124059 (2017).

[43] N. A. Collins, E. G. Adelberger, and C. D. Hoyle, Analytic expressions for gravitational inner multipole moments of elementary solids and for the force between two rectangular solids, Classical Quantum Gravity **23,** 5463 (2006).

[44] J. Stirling and S. Schlamminger, Closed form expressions for gravitational multipole moments of elementary solids, Phys. Rev. D **100,** 124053 (2019).

[45] C. Trenkel and C. C. Speake, Interaction potential between extended bodies, Phys. Rev. D **60,** 107501 (1999).

[46] C. D'Urso and E. G. Adelberger, Translation of multipoles for a $1/r$ potential, Phys. Rev. D **55,** 7970 (1997).

[47] M. P. Ross, J. Kissel, L. Datrier, and T. Mistry, NCal least-squares spectral analysis, LIGO DCC, 2021, https://dcc.ligo.org/LIGO-T2100103/public.

[48] J. O'Dell, M. Hillard, B. Moore, and E. Sanchez, Advanced LIGO quadruple suspension assembly, LIGO DCC, 2009, https://dcc.ligo.org/LIGO-D0901346/public.

[49] M. P. Ross, J. Kissel, L. Datrier, and T. Mistry, NCal penultimate mass contribution, LIGO DCC, 2021, https://dcc.ligo.org/LIGO-T2100095/public.

[50] P. Nguyen, R. Schofield, A. Effler, C. Austin, V. Adya, M. Ball, S. Banagiri, K. Banowetz, C. R. Billman, and C. Blair, Environmental noise in Advanced LIGO detectors, Classical Quantum Gravity **38,** 145001 (2021).

[51] T. Mistry, M. Ross, L. Datrier, P. Nguyen, R. Schofield, J. Kissel, and E. Daw, H1 NCal prototype: PEM coupling, LIGO DCC, 2021, https://dcc.ligo.org/LIGO-T2100221/public.

[52] M. P. Ross, J. Kissel, L. Datrier, and T. Mistry, NCal torque to force calculations, LIGO DCC, 2021, https://dcc.ligo.org/LIGO-T2100088/public.

[53] D. Bhattacharjee, Y. Lecoeuche, S. Karki, J. Betzwieser, V. Bossilkov, S. Kandhasamy, E. Payne, and R. L. Savage, Fiducial displacements with improved accuracy for the global network of gravitational wave detectors, Classical Quantum Gravity **38,** 015009 (2021).

[54] P. Raffai, G. Szeifert, L. Matone, Y. Aso, I. Bartos, Z. Márka, F. Ricci, and S. Márka, Opportunity to test non-newtonian gravity using interferometric sensors with dynamic gravity field generators, Phys. Rev. D **84,** 082002 (2011).

[55] S. Ballmer, S. Márka, and P. Shawhan, Feasibility of measuring the shapiro time delay over meter-scale distances, Classical Quantum Gravity **27,** 185018 (2010).

[56] A. G. Sullivan, D. Veske, Z. M. I. Bartos, S. Ballmer, P. Shawhan, and S. Márka, Can we use next-generation gravitational wave detectors for terrestrial precision measurements of shapiro delay?, Classical Quantum Gravity **37,** 205005 (2020).

[57] A. Kawasaki, Measurement of the newtonian constant of gravitation g by precision displacement sensors, Classical Quantum Gravity **37,** 075002 (2020).

[58] Q. Li, C. Xue, J.-P. Liu, J.-F. Wu, S.-Q. Yang, C.-G. Shao, L.-D. Quan, W.-H. Tan, L.-C. Tu, Q. Liu *et al.*, Measurements of the gravitational constant using two independent methods, Nature (London) **560,** 582 (2018).